

See discussions, stats, and author profiles for this publication at: <https://www.researchgate.net/publication/228059013>

# Nonequilibrium Phases of Nanoparticle Langmuir Films

ARTICLE in LANGMUIR · JUNE 2012

Impact Factor: 4.46 · DOI: 10.1021/la301764t · Source: PubMed

CITATIONS

10

READS

41

10 AUTHORS, INCLUDING:



[Karol Vegso](#)

Slovak Academy of Sciences

43 PUBLICATIONS 102 CITATIONS

[SEE PROFILE](#)



[Eva Majkova](#)

Slovak Academy of Sciences

206 PUBLICATIONS 860 CITATIONS

[SEE PROFILE](#)



[Martin Weis](#)

Slovak University of Technology in Bratislava

143 PUBLICATIONS 841 CITATIONS

[SEE PROFILE](#)



[O. Kononov](#)

European Synchrotron Radiation Facility

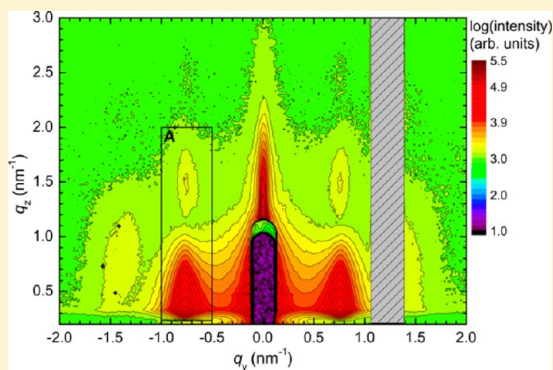
145 PUBLICATIONS 2,057 CITATIONS

[SEE PROFILE](#)

## Nonequilibrium Phases of Nanoparticle Langmuir Films

Karol Vegso,<sup>†</sup> Peter Siffalovic,<sup>\*,†</sup> Eva Majkova,<sup>†</sup> Matej Jergel,<sup>†</sup> Monika Benkovicova,<sup>†</sup> Teodora Kocsis,<sup>†</sup> Martin Weis,<sup>†</sup> Stefan Luby,<sup>†</sup> Kim Nygård,<sup>‡</sup> and Oleg Konovalov<sup>‡</sup><sup>†</sup>Institute of Physics, Slovak Academy of Sciences, Dubravská cesta 9, 845 11 Bratislava, Slovakia<sup>‡</sup>European Synchrotron Radiation Facility, BP 220, F-38043 Grenoble, France

**ABSTRACT:** We report on an in-situ observation of the colloidal silver nanoparticle self-assembly into a close-packed monolayer at the air/water interface followed by a 2D to 3D transition. Using the fast tracking GISAXS technique, we were able to observe the immediate response to the compression of the self-assembled nanoparticle layer at the air/water interface and to identify all relevant intermediate stages including those far from the equilibrium. In particular, a new nonequilibrium phase before the monolayer collapse via the 2D to 3D transition was found that is inaccessible by the competing direct space imaging techniques such as the scanning and transmission electron microscopies due to the high water vapor pressure and surface tension.



## I. INTRODUCTION

Chemically synthesized highly monodisperse nanoparticles are in the core of many novel and emerging applications.<sup>1,2</sup> One of their fascinating properties is the ability of spontaneous self-assembly into large arrays that offers an accessible route to design regular macroscopic nanoparticle layers.<sup>3–6</sup> In particular, freely floating self-assembled nanoparticle layers at the air/water interface also known as the nanoparticle Langmuir films in analogy to the molecular Langmuir films attract permanent attention. They offer an easy and uncomplicated way to obtain large-scale self-assembled templates of nanomaterials. For example, the nanoparticle templates of plasmonic nanoparticles provide a key to enhanced power conversion efficiency of future solar cells or may serve as unique substrates for the surface-enhanced Raman scattering spectroscopy. Here, the gold and silver nanoparticles with plasmon resonance in the visible or near-infrared parts of the electromagnetic spectrum are typically used.

Macroscopic physical quantities such as the surface pressure, refractive index, or surface potential of the assembled atoms, molecules, or larger nanocomplexes of Langmuir films are readily measurable. A detailed review on the pressure/temperature phase diagrams of metal nanoparticle monolayers at the air/water interface can be found in ref 7. A list of the analytical techniques applicable to the air/water interface studies includes the surface pressure and surface potential measurements, Brewster angle and fluorescence microscopy, surface plasmon resonance, imaging, and spectroscopic ellipsometry.<sup>8</sup> All these measurements track macroscopic behavior stimulated by the changes of the atomic and/or molecular order at micro- or nanoscale. The conventional direct space imaging methods that reveal the atomic/molecular order such as the scanning and transmission electron microscopy or nanoscale scanning probe techniques are inapplicable at the air/

water interfaces primarily due to the high vapor pressure and surface tension of the water subphase. On the other hand, the ex-situ studies of Langmuir nanoparticle films transferred onto solid substrates showed relaxation effects and are not suitable to reveal subtle changes in the formation of Langmuir films.<sup>9,10</sup> Here, the reciprocal space techniques based on the scattering of X-rays or neutrons prove to be unique in revealing the atomic or molecular structure details at the air/water interface.<sup>11</sup> The grazing incidence X-ray diffraction (GIXD) is established as the routine technique for structural studies of molecular Langmuir films.<sup>11,12</sup> For Langmuir films composed of nanoscale complexes such as nanoparticles, the reciprocal space required to analyze is shifted to the small-angle scattering region. Here the synchrotron-based GISAXS is the leading technique for providing the information on the order and size of the nanoscale objects forming Langmuir films.<sup>13,14</sup> Simultaneous application of the microscopic and macroscopic analytical techniques enables us to relate the structure evolution at nanoscale to the macroscopic behavior in terms of the surface pressure, refractive index, etc.

In this article, we report in detail on the principal stages of a plasmonic nanoparticle Langmuir film compression at the air/water interface followed by a pressure release. In particular, an immediate response of the nanoparticle order to the surface pressure evolution is monitored to be able to detect transient phenomena far from the equilibrium. The grazing-incidence small-angle X-ray scattering (GISAXS) technique is employed for a fast direct in-situ tracking of the process that is inaccessible by the competing real-space imaging techniques.<sup>13</sup> The Brewster angle microscopy and imaging ellipsometry are

Received: April 30, 2012

Revised: June 20, 2012

Published: June 23, 2012



used to support the experimental observations. Our study reveals a new nonequilibrium phase preceding the monolayer collapse that has not been reported yet. The implications for preparation of ordered nanoparticle templates by the Langmuir–Blodgett or Langmuir–Schaefer techniques are straightforward.

## II. EXPERIMENTAL SECTION

The in-situ GISAXS measurements at the air/water interface were performed at ID10B beamline at ERSF, Grenoble (France). The X-ray beam of the size  $300 \times 100 \mu\text{m}^2$  (HxV) and the energy 8 keV hit the air/water interface at  $0.35^\circ$  grazing angle of incidence. A fast 2D X-ray detector PILATUS 300 K was used to record the scattered X-ray radiation. The dead area between the detection modules of PILATUS 300 K is hatched in the reciprocal space maps. The reciprocal space calibration was done by the silver behenate standard. The Brewster angle microscopy and null ellipsometry images were acquired by a commercially available spectroscopic and laser imaging ellipsometer EP3SE (Accurion, Goettingen, Germany). The Langmuir nanoparticle films were prepared in a custom-designed Langmuir trough made of Teflon. The maximum and minimum subphase surface was 456 and 115  $\text{cm}^2$ , respectively. Milli-Q deionized water (specific electrical resistance  $>18 \text{ M}\Omega\text{-cm}$ ) was used as the subphase. We studied Langmuir film composed of spherical Ag nanoparticles capped with oleic acid and oleylamine surfactant. The chemical synthesis was published elsewhere.<sup>15</sup> The Ag nanoparticles with a concentration of 0.2 mg/mL dispersed in chloroform (99.8%, HPLC grade) were spread at the water subphase. After spreading the nanoparticles, the solvent was let to evaporate for 15 min before the measurement. The surfactant prevents the nanoparticles from agglomeration and is crucial for the formation of Langmuir film on the water subphase. The diameter of the Ag nanoparticle core of  $7 \pm 0.7 \text{ nm}$  was determined by the small-angle X-ray scattering (SAXS).

## III. RESULTS AND DISCUSSION

Figure 1 shows the GISAXS reciprocal space map of the nanoparticle Langmuir film at zero surface pressure integrated

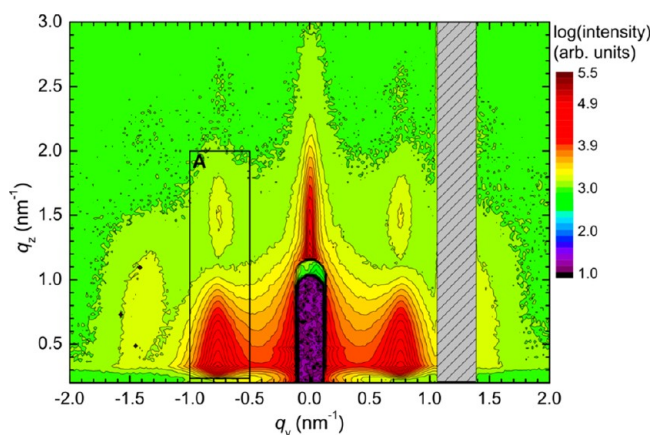


**Figure 1.** GISAXS reciprocal space map of Langmuir film at the air/water interface at zero surface pressure. The self-assembled islands of Ag nanoparticles produce the characteristic Bragg rods visible in the image. The area of the first Bragg rod denoted by A was used for the evaluation of the Bragg rod position and width.

for 100 s. The  $q_z$  and  $q_y$  are the normal and lateral (in-plane) components of the scattering vector with respect to the air/water interface. In the first approximation the measured reciprocal space map consists of the nanoparticle interference function which is modulated by the nanoparticle form factor function.<sup>13</sup> The nanoparticle interference function of an

ordered monolayer of monodisperse nanoparticles is reduced to a series of Bragg rods.<sup>16–18</sup> The first Bragg rod corresponds to the (10) diffraction from the two-dimensional (2D) nanoparticle submonolayer with hexagonal local order.<sup>17</sup> The higher order Bragg rods corresponding to the (11) and (20) diffractions are strongly suppressed due to a minimum in the form factor function.<sup>16</sup> They are visible only after a long integration time and at a dense nanoparticle coverage. The Fourier transform of the nanoparticle interference function provides the nanoparticle pair correlation function.<sup>19,20</sup> The form factor function depends on the nanoparticle shape and composition.<sup>20</sup> For a detailed simulation of the measured data one has to take into account the multiple scattering effects occurring at grazing incidence/exit angle that are treated in the distorted wave Born approximation (DWBA) theory.<sup>13,21</sup> At an incidence angle  $\alpha_i$  well above the critical angle  $\alpha_c$  ( $\alpha_i \sim 3\alpha_c$ ) and slowly varying nanoparticle form factor function, one can relate the mean hexagonal lattice spacing  $d_{10}$  to the first Bragg rod maximum position  $q_y^{\text{max}}$  as  $d_{10} = 2\pi/q_y^{\text{max}}$ .<sup>16,17</sup> Considering the monolayer of hexagonally ordered close-packed spherical nanoparticles, the maximum of the first Bragg rod located at  $q_y^{\text{max}} = 0.75 \text{ nm}^{-1}$  gives the nearest-neighbor interparticle distance  $\Delta = 9.7 \text{ nm}$  ( $\Delta = 2d_{10}/\sqrt{3}$ ).<sup>19</sup> Assuming the mean nanoparticle core diameter of 7 nm measured by SAXS, this gives some 1.4 nm for the surfactant shell thickness, which is in good agreement with the results published for the nanoparticles terminated with the identical surfactant molecules.<sup>17</sup> To track in situ the evolution of the nanoparticle order as a function of the surface pressure in the Langmuir trough during the compression and expansion at a constant barrier speed of 26  $\text{cm}^2/\text{min}$ , a continuous series of the GISAXS frames taken by a fast 2D detector were recorded as a movie. The time elapsed between the two successively recorded frames was 1.87 s, which was short enough to prevent from any relaxation effects and to reveal immediate response of Langmuir film to continuous compression and expansion. In order to reduce the statistical noise, five successive frames were integrated together. The measured surface pressure–area ( $\Pi$ – $A$ ) isotherm and surface elastic modulus  $E$  are shown in Figure 2a. The elastic modulus data were calculated as<sup>8</sup>

$$E = -A \left( \frac{d\Pi}{dA} \right) \quad (1)$$

where  $\Pi$  and  $A$  are the surface pressure and area, respectively. The Bragg rod maximum position and width (fwhm) as a function of the surface area are shown in Figures 2b and Figure 2c, respectively. For the Bragg rod evaluation, the intensity between  $q_z = 0.24 \text{ nm}^{-1}$  and  $q_z = 2 \text{ nm}^{-1}$  was integrated. The total integrated reciprocal space denoted by A is shown in Figure 1. Such a long integration along  $q_z$  is necessary as the compression of the nanoparticle layer redistributes the intensity along the Bragg rods (see below) that suggests formation of a vertically correlated second layer.<sup>16,21–23</sup> Moreover, the type of the vertical correlation of the nanoparticle positions can be elucidated directly from the intensity modulations along the Bragg rods as we have demonstrated recently.<sup>22</sup> Let us suppose a vertically correlated close-packed nanoparticle bilayer that is analogous to the AB layer stacking known from the crystallography of solids.<sup>24</sup> For such a stacking of spherical nanoparticles, the vertical lattice spacing  $d_z$  is given as  $\sqrt{6}\Delta/3$  where  $\Delta$  is the in-plane interparticle distance as given above.<sup>24</sup> The presence of the second nanoparticle layer in the AB stacking (hexagonally close-packed bilayer) is manifested in the



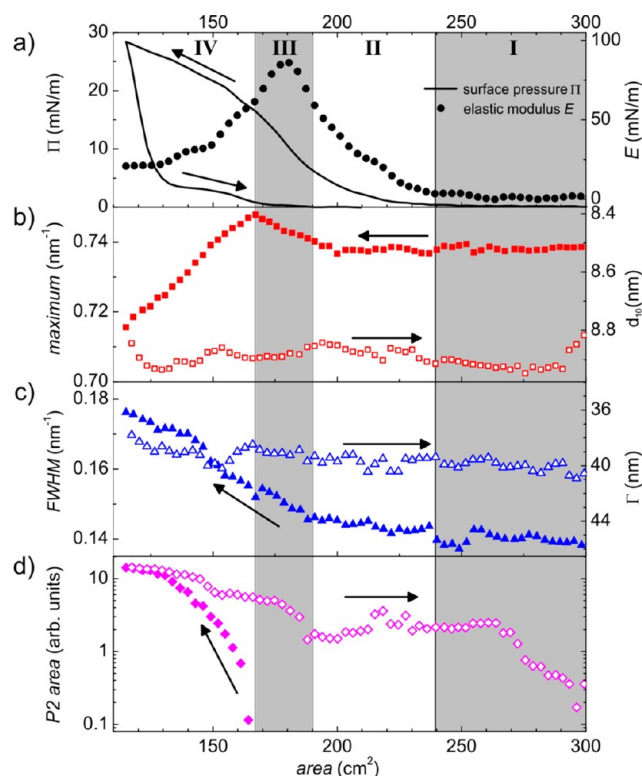


**Figure 2.** Major compression stages of the plasmonic nanoparticle Langmuir film. The arrows show the compression and expansion periods. The curves show dependence on the surface area of the following quantities. (a) The surface pressure  $\Pi$  and surface elastic modulus  $E$ . (b) The Bragg rod maximum position and the derived hexagonal lattice spacing  $d_{10}$ . (c) The Bragg rod width fwhm and the derived size of the coherently scattering domain of the nanoparticle crystal  $\Gamma$ . (d) The integral area of the peak P2 that is indicator of the newly formed nanoparticle bilayer with the AB-like stacking.

reciprocal space by the diffraction peaks  $P1(q_y, q_z)$  and  $P2(q_y, q_z)$  located at  $(0, 2\pi/d_z)$  and  $(2\pi/d_{10}, \pi/d_z)$ , respectively.<sup>22</sup> The peak P1 indicates the existence of the second layer without giving any particular information on its correlation with respect to the first one while the peak P2 is an unambiguous indicator of the AB-like nanoparticle stacking.<sup>16,22</sup> Taking the in-plane interparticle spacing  $\Delta = 9.7$  nm of the hexagonally ordered

monolayer calculated above from GISAXS, the peaks P1 and P2 should occur at  $q_z = 0.8$  nm<sup>-1</sup> and  $q_z = 0.4$  nm<sup>-1</sup>, respectively. Such peaks can be observed in the reciprocal space map during compression of the nanoparticle monolayer. The reciprocal space maps of the Langmuir film at zero surface pressure (submonolayer composed of the self-assembled nanoparticle islands) and at surface pressure of 28.4 mN/m (nanoparticle bilayer) are shown in Figure 3. In the former, the maximum intensity of the first Bragg rod is at the Yoneda peak,<sup>25</sup> i.e., at the critical exit angle. The modulation of the Bragg rod intensity is due to a minimum in the form factor function. In the latter, the second nanoparticle layer is formed with an additional vertical correlation corresponding to the AB crystallographic stacking. The bilayer is indicated by peaks P1 and P2 of the newly formed vertical interference function (Figure 3). The peak P1 is hidden behind the specular beamstop and brings information on the nanoparticle layering but not on a particular vertical nanoparticle correlation, i.e., on the type of the stacking. Such an information is provided by the peak P2. Its position matches perfectly that one calculated from the measured in-plane hexagonal lattice spacing if the AB stacking in the nanoparticle bilayer is supposed. Figure 2d shows the integral intensity under the peak P2 as a function of the nanoparticle Langmuir film area. The nonzero area under the peak P2 indicates formation of a nanoparticle bilayer with the AB-like stacking.

On the basis of the measured pressure–area isotherm and the X-ray scattering data, we can identify four principal stages of the nanoparticle Langmuir film compression that are indicated in Figure 2. In stage I, no measurable change in the surface pressure is detected. This behavior suggests similarity with the gaseous phase known in the molecular Langmuir films; however, there is a remarkable difference. In particular, we observe self-assembly of nanoparticles evidenced by the presence of Bragg rods in the reciprocal space map from the very beginning at zero surface pressure (Figure 1). Presumably a submonolayer composed of isolated self-assembled nanoparticle islands with translational mobility along the air/water interface is formed.<sup>26</sup> This mobility is documented by random island movement, resulting in instability of the Bragg rod intensity (not shown here). The elastic modulus  $E$  is also formally evaluated in this compression stage; however, it has no physical meaning as the freely floating nanoparticle islands are

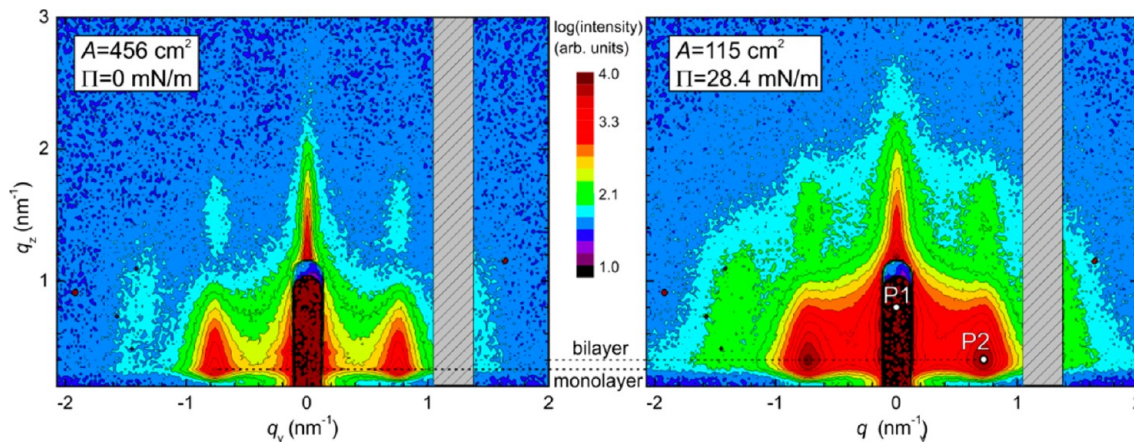


**Figure 3.** Reciprocal space maps of the nanoparticle Langmuir film at the surface pressure 0 mN/m (left) and 28.4 mN/m (right). The peaks P1 and P2 are associated with the AB stacked bilayer. The integration time for both maps was 9.4 s.

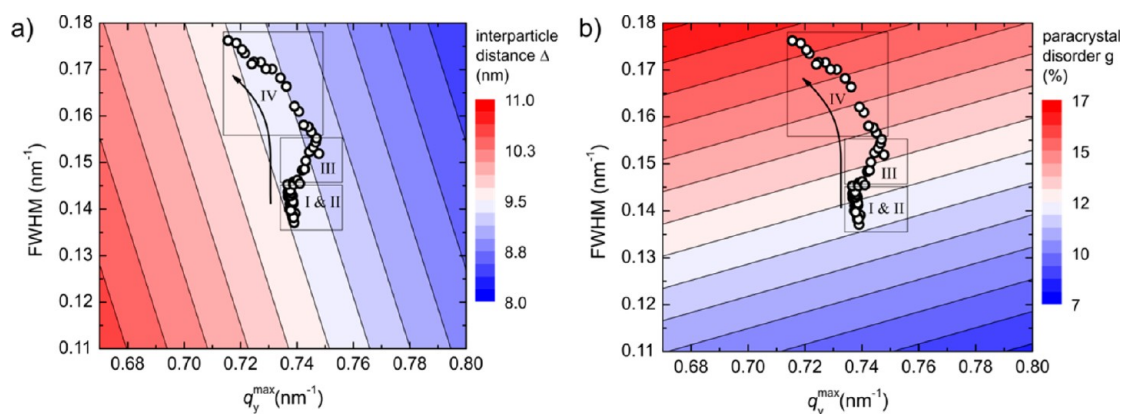


**Figure 4.** Numerical simulations of the (a) interparticle distance and (b) paracrystal disorder as a function of the Bragg rod maximum position and width in the reciprocal space based on the paracrystal model and DWBA theory. The open dots are the experimental points as shown in Figure 2b,c. The arrow represents the compression direction. The Roman letters indicate compression stages of the nanoparticle Langmuir film.

not interconnected to form a continuum. The nanoparticle islands coalesce gradually into larger assemblies during the compression as indicated further also by the Brewster microscopy. This process takes place without a distinct measurable change in the Bragg rod maximum position and width (Figure 2b,c) which implies preserved nanoparticle order in the coalesced islands.<sup>16</sup> The reduction of the Bragg rod width was not observed because of a restricted size of the coherently scattering domains (Figure 2c) in the pristine islands controlled by the nanoparticle cumulative disorder. In stage II, we observe a steady increase in the surface pressure and surface elastic modulus (Figure 2a). Here the proceeding island coalescence during the barrier movement forces gradually the larger assemblies to get into contact. This process results in stress accumulation at the assembly boundaries that is relieved by the nanoparticle rearrangements in these regions to form a continuous close-packed monolayer with local hexagonal order preserved from the original islands. Such a scenario is supported by the nearly unchanged Bragg rod maximum position and width during stage II (Figure 2b,c). The nanoparticle Langmuir film at the end of stage II is suitable for the transfer onto a solid substrate to deposit a high-quality nanoparticle monolayer over large area as we documented by the scanning electron microscopy.<sup>27</sup> We can compare this stage to the liquid-expanded phase of the molecular Langmuir films.<sup>9</sup> In stage III, we observe a steeper increase in the surface pressure followed by a maximum in the surface elastic modulus. Using computer simulations, it was shown that such a maximum precedes formation of the second nanoparticle layer.<sup>28</sup> The isotherm behavior in stage III is analogous to the liquid-condensed phase of the molecular Langmuir films.<sup>9</sup> A shift in the Bragg rod maximum position to the higher  $q_y$  values suggests a decrease in the lattice spacing  $d_{10}$  by  $\sim 0.1$  nm (Figure 2b) while a simultaneous increase in the Bragg rod width (Figure 2c) indicates a deterioration of the nanoparticle order due to the accumulated stress. Such a Bragg rod behavior can be explained by a slight compressive deformation of the nanoparticle capping surfactant shell. This nonequilibrium nanoparticle compression phase can be observed only at a continuous Langmuir film compression and was not observed under the steady-state conditions.<sup>16,18,29</sup> In stage IV, the peak P2 appears and grows as the indicator of a newly formed second nanoparticle layer.<sup>21,22</sup> The second layer formation and consequent stress relief in the first one result in the reversed

shift of the Bragg rod maximum position that indicates increase in the  $d_{10}$  lattice spacing. The Bragg rod width increases as well suggesting growing disorder, presumably due to the defect creation in the first nanoparticle layer when the second one is formed.<sup>16</sup> Such a growth of the lattice spacing with the growing disorder is typical for the paracrystal model of nanoparticle assemblies.<sup>20</sup> In the limit of highly disordered paracrystal the Bragg rod maximum position  $q_y^{\max}$  is controlled by the interparticle distance  $\Delta$  instead of the lattice spacing  $d_{10}$ ; i.e.  $q_y^{\max} = 2\pi/\Delta$  instead of  $q_y^{\max} = 2\pi/d_{10}$ .<sup>17,20</sup> The Bragg rod maximum position at the end of stage IV is between these values that suggests partial paracrystalline disorder.

A comprehensive simulation of the nanoparticle Langmuir film based on the paracrystal model was carried out by the numerical code described in ref 21. Briefly, the numerical simulation was based on a 2D paracrystal composed of 400 nanoparticles. The azimuthally averaged interference function of the nanoparticle monolayer was used in the simulation of the Bragg rod applying the full DWBA theory. Relying on this model, the paracrystal interparticle distance  $\Delta$  and paracrystal disorder  $g$  can be calculated as a function of the Bragg rod maximum position and width (fwhm) at the critical exit angle (Figure 4). The experimental values of the Bragg rod position and width can be readily overlapped with this simulated paracrystal landscape that gives an intuitive insight into the undergoing paracrystal transformations during the film compression. The stages I and II are represented by a constant interparticle distance. A minor change in the Bragg rod width in stage II can be viewed as a slight increase of the paracrystal disorder due to the stress accumulated at the nanoparticle boundaries of the interconnected nanoparticle islands. The transient compression stage III can be clearly seen as an increase of the paracrystal disorder by 1% accompanied by a reduction of the interparticle distance by 0.2 nm. The formation of the second nanoparticle layer in stage IV recovers the original interparticle distance as the stress accumulated in the first layer is relieved by displacing some nanoparticles into the second one. The accompanying defect formation in the first nanoparticle layer increases the paracrystal disorder by some 2%. An increased disorder in the collapsed nanoparticle films at the air/water interface was reported also previously.<sup>7</sup>

The Brewster angle microscopy images are presented in Figure 5. The images taken at the surface pressures 5 and 9 mN/m in stage II are characterized by the coalesced



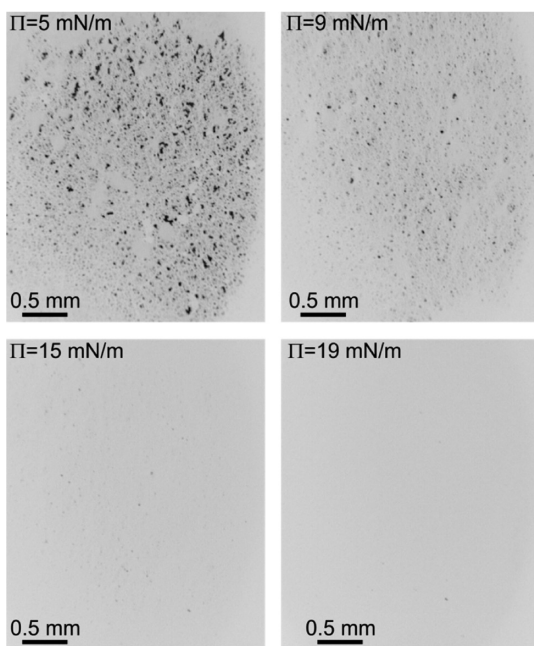


**Figure 5.** Brewster angle microscopy images taken at the indicated surface pressures demonstrate the transition from a submonolayer to a continuous nanoparticle monolayer.

nanoparticle islands.<sup>18,26</sup> The increasing surface pressure closes the voids in the nanoparticle island network. The image taken at the surface pressure of 15 mN/m belongs to stage III and shows a large continuous nanoparticle monolayer. Further increase in the surface pressure to 19 mN/m results in the second nanoparticle layer formation that is not visible in the Brewster angle microscopy. In contrast to Brewster angle microscopy, the imaging null ellipsometry offers flexibility in eliminating the reflected light from an arbitrary layer of a constant thickness at the air/water interface. Figure 6 shows

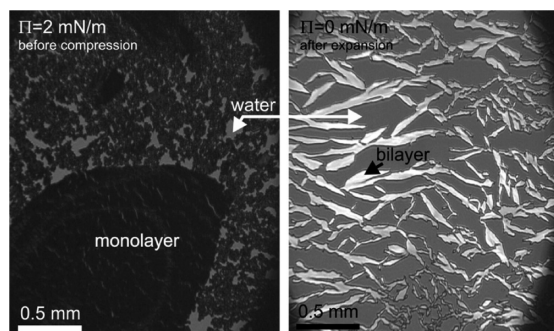


**Figure 6.** Null ellipsometry images of the nanoparticle Langmuir film before the compression and after the expansion. The null imaging ellipsometer was configured to stop the polarized light reflected from the nanoparticle monolayer.

two images of the nanoparticle Langmuir film before the compression and after the expansion. The polarizer and analyzer rotations of the imaging ellipsometer were set to the values that discriminate the light reflected from the monolayer nanoparticle islands. The nanoparticle monolayer appears to be black with these ellipsometer settings. Contrarily, the light reflected from the water subphase and the nanoparticle bilayer formed in stage IV passes the analyzer and is visualized by various shades of gray in Figure 6. At the surface pressure of 2

mN/m we clearly observe small and large nanoparticle islands composed of the nanoparticle monolayer. With the increasing surface pressure the nanoparticle islands are continuously coalesce and form a close-packed continuous nanoparticle monolayer.<sup>18,26</sup> The surface pressure above the critical value for the monolayer collapse leads to the formation of the nanoparticle bilayer.<sup>16</sup> The expansion of bilayer area results in the generation of cracks in the compressed film that is followed by a full disintegration into needle-like bilayer islands. Such an irreversible behavior is shown in the second image in Figure 6 where highly reflective needle-like bilayer islands can be seen. If the nanoparticles in islands relaxed into monolayers, the reflected light would be extinguished by the analyzer and the islands would appear black in the image.

Formation of the bilayer was confirmed also by our atomic force microscopy (AFM) studies of the Ag nanoparticle films transferred onto solid substrates in stage IV of the isotherm.<sup>30</sup> We observed a similar compression behavior and bilayer formation for the iron oxide and cobalt–iron oxide nanoparticle Langmuir films with the identical oleic acid and oleylamine surfactant. On the other hand, GISAXS studies of the Au thiol-capped nanoparticle film performed at equilibrium conditions and with a smaller compression speed revealed only a monolayer buckling manifested by bending the Bragg rods.<sup>10,31</sup> Similarly, the AFM studies of the Au thiol-capped nanoparticle films transferred onto solid substrates reported on the monolayer collapse via film folding followed by a trilayer formation.<sup>31</sup> Therefore, the surfactant type obviously affects the nanoparticle monolayer behavior at high surface pressures.<sup>26</sup> It has been also argued that faster compression speed favors the monolayer collapse and bilayer formation.<sup>10</sup> One has to be aware of the fact that the transitions between particular compression stages do not occur simultaneously across the whole nanoparticle Langmuir film. Therefore, different phases coexist, similarly to the molecular Langmuir films.<sup>12</sup> A hysteretic behavior of the pressure–area isotherm during the film expansion indicates that bilayer formation is irreversible (Figure 2a). The identical irreversible behavior was reported on Au thiol-capped nanoparticle films.<sup>32</sup> The Bragg rod maximum position and width are not recovered during the film expansion, suggesting the stable nanoparticle order in the bilayer. The drop in the P2 peak area may be explained by decreasing amount of nanoparticles in the probed X-ray volume during the film expansion when the bilayer islands are formed and go away from each other, leaving free subphase surface behind.

#### IV. CONCLUSIONS

In this article we identified the principal formation stages of the Ag nanoparticle Langmuir film using the in-situ X-ray scattering technique supported by Brewster angle microscopy and imaging ellipsometry. The formation of nanoparticle monolayer takes place via coalescence of free self-assembled nanoparticle islands with the hexagonal close-packed order at early compression stage. The original nanoparticle order persists in the coalesced assemblies up to a temporary squeezing of the hexagonal lattice shortly before the monolayer collapse that has not been observed before. The collapse takes place by flipping up the nanoparticles and the second layer formation with the AB-like crystallographic stacking and enhanced paracrystalline-like disorder. The Langmuir film expansion runs irreversibly by decomposition into bilayer islands without observable changes in the nanoparticle order inside.

## AUTHOR INFORMATION

### Corresponding Author

\*Tel +421-2-20910766; e-mail peter.siffalovic@savba.sk.

### Notes

The authors declare no competing financial interest.

## ACKNOWLEDGMENTS

This work was done during implementation of the project Applied Research of Advanced Photovoltaic Cells, ITMS code 26240220047 (50%), supported by the Research and Development Operational Programme funded by the ERDF. The support of the Grant Agency VEGA Bratislava, project No. 2/0041/11, Slovak Research and Development Agency, project No. APVV LPP-0175-09, and project Centre of Excellence SAS for Functionalized Multiphase Materials FUN-MAT is also acknowledged.

## REFERENCES

- (1) Park, J.; An, K. J.; Hwang, Y. S.; Park, J. G.; Noh, H. J.; Kim, J. Y.; Park, J. H.; Hwang, N. M.; Hyeon, T. Ultra-large-scale syntheses of monodisperse nanocrystals. *Nat. Mater.* **2004**, *3* (12), 891–895.
- (2) Sun, S. H.; Murray, C. B.; Weller, D.; Folks, L.; Moser, A. Monodisperse FePt nanoparticles and ferromagnetic FePt nanocrystal superlattices. *Science* **2000**, *287* (5460), 1989–1992.
- (3) Bigioni, T. P.; Lin, X. M.; Nguyen, T. T.; Corwin, E. I.; Witten, T. A.; Jaeger, H. M. Kinetically driven self assembly of highly ordered nanoparticle monolayers. *Nat. Mater.* **2006**, *5* (4), 265–270.
- (4) Martin, M. N.; Basham, J. I.; Chando, P.; Eah, S. K. Charged Gold Nanoparticles in Non-Polar Solvents: 10-min Synthesis and 2D Self-Assembly. *Langmuir* **2010**, *26* (10), 7410–7417.
- (5) Shevchenko, E. V.; Talapin, D. V.; Kotov, N. A.; O'Brien, S.; Murray, C. B. Structural diversity in binary nanoparticle superlattices. *Nature* **2006**, *439* (7072), 55–59.
- (6) Talapin, D. V.; Shevchenko, E. V.; Bodnarchuk, M. I.; Ye, X. C.; Chen, J.; Murray, C. B. Quasicrystalline order in self-assembled binary nanoparticle superlattices. *Nature* **2009**, *461* (7266), 964–967.
- (7) Heath, J. R.; Knobler, Ch. M.; Leff, D. V. Pressure/Temperature Phase Diagrams and Superlattices of Organically Functionalized Metal Nanocrystal Monolayers: The Influence of Particle Size, Size Distribution, and Surface Passivant. *J. Phys. Chem. B* **1997**, *101*, 189–197.
- (8) Barnes, G.; Gentle, I. *Interfacial Science: An Introduction*; Oxford University Press: New York, 2005.
- (9) Banerjee, R.; Hazra, S.; Banerjee, S.; Sanyal, M. K. Nanopattern formation in self-assembled monolayers of thiol-capped Au nanocrystals. *Phys. Rev. E* **2009**, *80* (5).
- (10) Banerjee, R.; Sanyal, M. K.; Bera, M. K.; Singh, A.; Novak, J.; Kononov, O. Structural reordering in monolayers of gold nanoparticles during transfer from water surface to solid substrate. *Phys. Rev. E* **2011**, *83* (5).
- (11) Kaganer, V. M.; Mohwald, H.; Dutta, P. Structure and phase transitions in Langmuir monolayers. *Rev. Mod. Phys.* **1999**, *71* (3), 779–819.
- (12) Mowald, H. Surfactant Layers at Water Surfaces. *Rep. Prog. Phys.* **1993**, *56* (5), 653–685.
- (13) Renaud, G.; Lazzari, R.; Leroy, F. Probing surface and interface morphology with Grazing Incidence Small Angle X-Ray Scattering. *Surf. Sci. Rep.* **2009**, *64* (8), 255–380.
- (14) Renaud, G.; Lazzari, R.; Revenant, C.; Barbier, A.; Noblet, M.; Ulrich, O.; Leroy, F.; Jupille, J.; Borensztein, Y.; Henry, C. R.; Deville, J. P.; Scheurer, F.; Mane-Mane, J.; Fruchart, O. Real-time monitoring of growing nanoparticles. *Science* **2003**, *300* (5624), 1416–1419.
- (15) Vegso, K.; Siffalovic, P.; Weis, M.; Jergel, M.; Benkovicova, M.; Majkova, E.; Chitu, L.; Halahovets, Y.; Luby, S.; Capek, I.; Satka, A. In situ GISAXS monitoring of Langmuir nanoparticle multilayer degradation processes induced by UV photolysis. *Phys. Status Solidi A* **2011**, *208* (11), 2629–2634.
- (16) Fukuto, M.; Heilmann, R. K.; Pershan, P. S.; Badia, A.; Lennox, R. B. Monolayer/bilayer transition in Langmuir films of derivatized gold nanoparticles at the gas/water interface: An X-ray scattering study. *J. Chem. Phys.* **2004**, *120* (7), 3446–3459.
- (17) Heitsch, A. T.; Patel, R. N.; Goodfellow, B. W.; Smilgies, D. M.; Korgel, B. A. GISAXS Characterization of Order in Hexagonal Monolayers of FePt Nanocrystals. *J. Phys. Chem. C* **2010**, *114* (34), 14427–14432.
- (18) Schultz, D. G.; Lin, X.-M.; Li, D.; Gebhardt, J.; Meron, M.; Viccaro, J.; Lin, B. Structure, Wrinkling, and Reversibility of Langmuir Monolayers of Gold Nanoparticles. *J. Phys. Chem. B* **2006**, *110* (48), 24522–24529.
- (19) Als-Nielsen, J.; MacMorrow, D. *Elements of Modern X-ray Physics*, 2nd ed.; Wiley: Chichester, 2011.
- (20) Lazzari, R. Grazing Incidence Small-Angle X-Ray Scattering from Nanostructures. In *X-ray and Neutron Reflectivity*; Daillant, J., Gibaud, A., Eds.; Springer: Berlin, 2009; Vol. 770, pp 283–342.
- (21) Vegso, K.; Siffalovic, P.; Jergel, M.; Weis, M.; Benkovicova, M.; Majkova, E.; Luby, S.; Kocis, T.; Capek, I. Silver nanoparticle monolayer to bilayer transition at the air/water interface studied by GISAXS technique - application of a new paracrystal model. *Langmuir* **2012**, DOI: 10.1021/la301577a.
- (22) Vegso, K.; Siffalovic, P.; Benkovicova, M.; Jergel, M.; Luby, S.; Majkova, E.; Capek, I.; Kocis, T.; Perlich, J.; Roth, S. V. GISAXS analysis of 3D nanoparticle assemblies—effect of vertical nanoparticle ordering. *Nanotechnology* **2012**, *23* (4), 045704.
- (23) Smilgies, D. M.; Heitsch, A. T.; Korgel, B. A. Stacking of Hexagonal Nanocrystal Layers During Langmuir-Blodgett Deposition. *J. Phys. Chem. B* **2012**, *116* (20), 6017–6026.
- (24) Hammond, C. *The Basics of Crystallography and Diffraction*, 3rd ed.; Oxford University Press: New York, 2010.
- (25) Yoneda, Y. Anomalous Surface Reflection of X Rays. *Phys. Rev.* **1963**, *131* (5), 2010.
- (26) Lin, B.; Schultz, D. G.; Lin, X.-M.; Li, D.; Gebhardt, J.; Meron, M.; Viccaro, P. J. Langmuir monolayers of gold nanoparticles. *Thin Solid Films* **2007**, *515* (14), 5669–5673.
- (27) Siffalovic, P.; Chitu, L.; Majkova, E.; Vegso, K.; Jergel, M.; Luby, S.; Capek, I.; Satka, A.; Maier, G. A.; Keckes, J.; Timmann, A.; Roth, S. V. Kinetics of Nanoparticle Reassembly Mediated by UV-Photolysis of Surfactant. *Langmuir* **2010**, *26* (8), 5451–5455.
- (28) Kubowicz, S.; Hartmann, M. A.; Daillant, J.; Sanyal, M. K.; Agrawal, V. V.; Blot, C.; Kononov, O.; Möhwald, H. Gold Nanoparticles at the Liquid–Liquid Interface: X-ray Study and Monte Carlo Simulation. *Langmuir* **2008**, *25* (2), 952–958.
- (29) Bera, M. K.; Sanyal, M. K.; Pal, S.; Daillant, J.; Datta, A.; Kulkarni, G. U.; Luzet, D.; Kononov, O. Reversible buckling in monolayer of gold nanoparticles on water surface. *Europhys. Lett.* **2007**, *78* (5).
- (30) Siffalovic, P.; Majkova, E.; Jergel, M.; Vegso, K.; Weis, M.; Luby, S. Self-assembly of nanoparticles at solid and liquid surfaces. In *Smart Nanoparticles Technology*; Hashim, A., Ed.; INTECH: Rijeka, 2012.
- (31) Leahy, B. D.; Pocivavsek, L.; Meron, M.; Lam, K. L.; Salas, D.; Viccaro, P. J.; Lee, K. Y. C.; Lin, B. H. Geometric Stability and Elastic Response of a Supported Nanoparticle Film. *Phys. Rev. Lett.* **2010**, *105* (5).
- (32) Kundu, S. Layer-by-Layer Assembly of Thiol-Capped Au Nanoparticles on a Water Surface and Their Deposition on H-Terminated Si(001) by the Langmuir-Blodgett Method. *Langmuir* **2011**, *27* (7), 3930–3936.